PCCP
Physical Chemistry Chemical Physics

Accepted Manuscript

This article can be cited before page numbers have been issued, to do this please use: C. Salguero and S. A. Lopez, *Phys. Chem. Chem. Phys.*, 2026, DOI: 10.1039/D6CP00519E.

ROYAL SOCIETY OF CHEMISTRY

rsc.li/pccp

View Article Online
DOI: 10.1039/D6CP00519E

Multiconfigurational non-adiabatic molecular dynamics towards photochemical-N_2-extrusion reactions in borodiazenes

Christian Salguero and Steven A. Lopez*

Department of Chemistry and Chemical Biology, Northeastern University, Boston, Massachusetts, 02115, United States

*Corresponding author: s.lopez@northeastern.edu

Abstract

We used state-of-the-art quantum-chemical calculations to study the photodenitrogenation of 1-methylborodiazene to 1-methylborirane. Vertical excitation energy calculations indicate that the $S_0 \rightarrow S_1$ ($n_N \rightarrow \pi^*_{NN}$) and $S_0 \rightarrow S_2$ ($n_N \rightarrow 2p_B$) transitions are accessible (318 nm and 287 nm, respectively), and the $S_0 \rightarrow S_1$ transition is the bright state. The minimum-energy path indicates near-degeneracy between the S_1 and S_2 surfaces in the Franck-Condon region, leading to the steepest descent path on the S_1 state to be towards fluorescent decay rather than denitrogenation. Our simulations indicate that denitrogenation primarily occurs shortly after an S_1/S_0 hopping event (79% of trajectories) and proceeds via three distinct pathways. The dominant pathway involves boron pyramidalization and partial π_{NN} isomerization in the S_1 state, with N_2 elimination shortly after an S_1/S_0 hop. Minor pathways include either π_{NN} isomerization or boron pyramidalization, with N_2 elimination occurring on the S_0 and S_1 states, respectively. We also observed that some trajectories rearrange to form a diazoborete intermediate. Our results show that the labile N_2 group can be used to access base-free boriranes.

Introduction

Photochemistry exemplifies principles of green chemistry by utilizing renewable solar energy to facilitate reactions under mild conditions. Light activation enables spatiotemporal control over the activation and deactivation of chemical processes, such as cycloadditions[1-3], isomerizations[4-6], and gas evolutions[7-9]. These processes have excellent atom economy, minimal energy use, and high selectivity—traits that are highly valued in chemistry[10-12], biology[13-15], and materials science[1, 16-18]. Photochemical activation provides access to reactive intermediates that would otherwise be thermally inaccessible by breaking[19-21] and forming bonds[22-24], causing isomerizations[25], and altering electronic properties (*e.g.,* aromaticity/antiaromaticity[26-28]). These light-triggered modifications have led to the application of these reactions in energy storage[1, 16, 29], drug delivery[30-32], and total organic synthesis[33-35].

These photochemical reactions are used in organic synthesis to introduce ring strain[23, 36, 37] into chemical systems that would otherwise be kinetically or thermally unfavorable. Researchers can then utilize these ring-strained compounds in additional chemical reactions to produce final products, such as grazoprevir[38], 2-pyridylethylamine[39], and lasalocid[40].[33, 37, 41] Three-membered rings, such as cyclopropanes[42], aziridines[43], and epoxides/oxiranes[40, 44, 45] have garnered significant interest because of their distinctive reactivity, arising from inherent ring strain, which enables diverse synthetic applications.[41, 45, 46] Despite the high ring strain, these three-member rings are commonly found in natural products[47-49], leading to increased interest in pharmaceutical chemistry[43] and chemical biology[44, 50] (Figure 1).

View Article Online
DOI: 10.1039/D6CP00519E

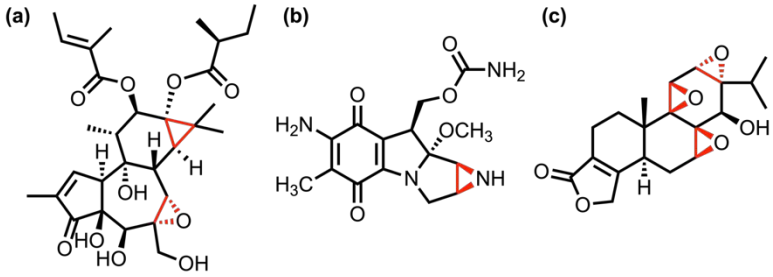

Figure 1. Examples of cyclopropanes, aziridines, and oxiranes within pharmaceutical agents: (**a**) triglanol tiglate[47], (**b**) aziridines mitosol[49] , and (**c**) triptolide[51], respectively. The three-membered rings are highlighted in red within the structures.

The synthetic methods for these rings include cyclopropanations[52-54], aziridination[53, 55-57], and epoxidations[53, 58], each of which produces its respective three-membered ring and is well-established. The widespread application of aziridines and oxiranes has driven research into other hetero-analogues of cyclopropanes, such as thiiranes[59-61], phosphiranes[62-64], and siliranes[65-67].[36] Like cyclopropanes, aziridines, and oxiranes, these compounds are highly reactive, often undergoing ring-opening reactions with nucleophiles[62, 65] or ring expansions with π-systems[67-69]. As a result, these three-membered rings have found uses in pharmaceutical chemistry[68, 70] and polymer synthesis[62, 65]. One hetero-analogue of cyclopropane, whose chemistry is not fully understood, is borirane, the boron analogue.

Pioneering work on the synthesis of borirane was conducted by Berndt and co-workers in 1983, in which the first B=C double bond was reported (Figure 2a).[73] Boriranes are highly reactive due to their ring strain and Lewis acidity.[74, 75] In 1991, Denmark and coworkers further expanded the field by introducing the first report of a Lewis base-stabilized borirane through the photoirradiation of diphenyl-(*E*)-2-phenylethenyl-borane (Figure 2b).[76]

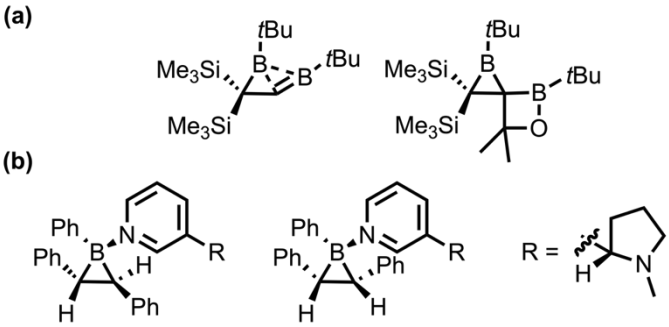

Figure 2. Comparison between the first **(a)** base-free borirane and **(b)** base-stabilized borirane.

In the late 2000s, Wang reported several *N,C*-chelated[77, 78] and *N*-heterocyclic carbene chelated boriranes[79] (NHC-borirane) for potential use in optoelectronic and organic synthesis, stemming from their easy and reversible C-C/C-B bond rearrangements triggered by both light and heat. Braunschweig *et al.* reported the synthesis of NHC-boriranes through the salt elimination of NHC-dichloroboranes with the dianion of *trans*-stilbene towards *trans*-1,2,3-triphenyl NHC-boriranes.[80] Curran and coworkers later reported a high-yield (80%) novel synthetic approach to NHC-boriranes via double hydroboration of acetylenedicarboxylates with NHC-boranes.[75] The NHC-boriranes show exceptional inertness in gas-phase, aqueous, thermal, and photolytic conditions because of the Lewis base stabilization.[72, 75, 80] In 2019, Curran *et al*. reported the first ring-opening reaction of base-stabilized borirane towards a novel class of NHC-boralactones.[81] Recent works have reported access to borirane derivatives, such as carborane-fused boriranes[82, 83], which have expanded the range of ligated boriranes. Nonetheless, base-free boriranes remain difficult to isolate.

Previous synthetic works have utilized denitrogenation reactions to synthesize three-member rings (*i.e.,* cyclopropanes[11, 84, 85], aziridines[86], oxiranes[87], and thiiranes[88, 89]). Similarly, Dowd described the photodenitrogenation of a five-membered ring, 4-methylene-Δ-pyrazoline, targeting the formation of trimethylenemethane; this highly reactive intermediate rapidly cyclized to produce cyclopropane at temperatures > 77K (Scheme 1a).[84] Here, we present a proof of concept for using the labile azo group in a similar denitrogenation reaction toward a base-free borirane. We

View Article Online
DOI: 10.1039/D6CP00519E

hypothesize that irradiation of a boron derivative of 4-methylene-Δ-pyrazoline, 1-borodiazene (**bd**), would promote N_2 extrusion and produce 1-methylborirane, **5** (Scheme 1b).

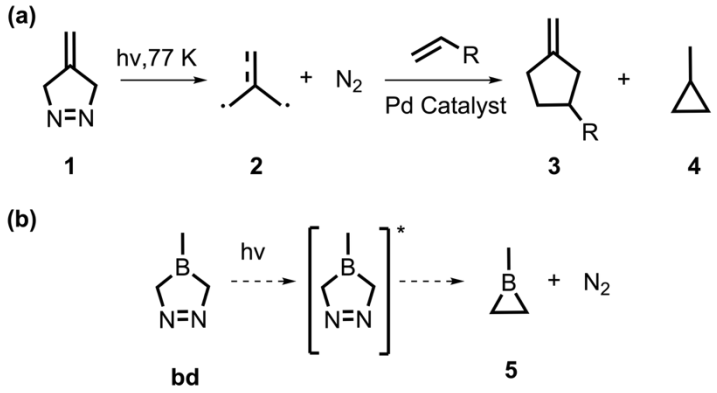

Scheme 1. (a) Photodenitrogenation of 4-methylene-Δ-pyrazoline towards a 1,3-diyl and subsequent cycloaddition towards functionalized five-member ring (**3**) and/or ring-closure towards methyl-cyclopropane (**4**). **(b)** Proof-of-concept photodenitrogenation reaction of 1-methyl-borodiazene (**bd**) towards base-free 1-methylborirane (**5**).

We conducted a computational investigation of the denitrogenation mechanism of **bd** using multiconfigurational (complete active space self–consistent field, CASSCF) and single-reference (time-dependent density functional theory, TD-DFT) quantum chemical methods. In this study, we comprehensively outlined the reaction pathways for the photochemical N_2 extrusion of **bd** towards **5** using our open-source Python rapid artificial intelligence ab initio molecular dynamics (PyRAI^{2}MD), which enabled quantum-mechanical nonadiabatic molecular dynamics (QM-NAMD).

Results and Discussion

Active space and characterization of excitation on the optimized global minimum

The first step in the proposed photochemical denitrogenation is the absorption of a photon by **bd**, inducing electronic excitation. Therefore, we initially calculated the photophysical properties—vertical excitation energies and nature of transitions—using TD-DFT and EOM-CCSD. We carried out TD-DFT calculations using CAM-B3LYP-GD3(BJ) and ωB97X-D with the cc-pVDZ basis set. The predicted vertical excitation energy for the ground-state-optimized structure of **bd**, designated as **bd-S$_0$**, was calculated to be 3.71 eV with CAM-B3LYP-GD3(BJ)/cc-pVDZ and 3.72 eV with ωB97X-D/cc-pVDZ. Both methods indicated that the $S_0 \rightarrow S_1$ excitation is a $n_N \rightarrow \pi^*_{NN}$ transition, with an oscillator strength of 0.003. To ensure the reliability of our TD-DFT results and due to the absence of experimental spectra, we compare them with EOM-CCSD calculations, which are considered the gold standard[25, 26] in the photochemistry community for single-reference excited-state calculations.[26, 27] We calculated the $S_0 \rightarrow S_1$ vertical excitation energy to be 4.07 eV using EOM-CCSD/cc-pVDZ. These results demonstrate that the TD-DFT values are 0.36 eV and 0.35 eV lower in energy than the EOM-CCSD values (CAM-B3LYP-GD3(BJ)/cc-pVDZ and ωB97X-D/cc-pVDZ, respectively). This difference suggests that TD-DFT methods tend to underestimate the vertical excitation energies of **bd-S$_0$** compared with EOM-CCSD. The multiconfigurational electronic structure of **bd-S$_0$** during photoexcitation and photodynamic simulations requires multiconfigurational quantum-mechanical methods to yield more accurate energetic descriptions.

As a result, we employed the complete active space self-consistent field (CASSCF) method and its second-order perturbation theory (CASPT2), both of which necessitate an active space. We examined the orbital transitions predicted by TD-DFT and EOM-CCSD, as well as those involved in the photodenitrogenation of **bd,** to identify which orbitals to incorporate into the active space. We included twelve electrons distributed across 11 orbitals in the active space of **bd**; Figure S1 shows the orbitals and their average orbital occupancy.

We compared the CASSCF and CASPT2 excitation energies and orbital transitions with those computed using single-reference methods (*i.e.,* TD-DFT and EOMCCSD) to ensure an accurate characterization of vertical excitation energies with the CAS(12,11) active space. When the vertical excitation energies and the nature of the transitions align between multiconfigurational and single-reference methods, this indicates that the selected active space effectively captures

View Article Online
DOI: 10.1039/D6CP00519E

the photophysical properties of the system of interest (*i.e.,* **bd-S$_0$**). Conversely, mismatches between the methods suggest that the selected active space is inadequately capturing the photophysical properties, and a new active space is needed. Due to the lack of experimental spectra for **bd**, we used the gold-standard[26] EOM-CCSD method as a reference. The vertical excitation energy for **bd-S$_0$** was calculated using state-averaged CAS(12,11) over the first five singlet states with the cc-pVDZ basis set (*i.e.,* SA5-CASSCF(12,11)/cc-pVDZ) to be 4.50 eV. This indicates that the SA5-CASSCF(12,11)/cc-pVDZ method overestimates the $S_0 \rightarrow S_1$ vertical excitation energy by 0.43 eV compared to EOM-CCSD/cc-pVDZ results. Additionally, it overestimates the $S_0 \rightarrow S_1$ vertical excitation energy relative to CAM-B3LYP-GD3BJ/cc-pVDZ and ωB97X-D/cc-pVDZ by 0.79 and 0.78, respectively. The discrepancies observed in the SA5-CASSCF(12,11)/cc-pVDZ calculation and single-reference methods arise from the omission of dynamical correlation in the former, which the CASPT2 method corrects. For the CASPT2 correction, the calculation was performed as SA5-CASPT2(12,11)/cc-pVDZ//SA5-CASSCF(12,11)/cc-pVDZ; the $S_0 \rightarrow S_1$ vertical excitation energy was 3.90 eV. This value is 0.17 eV lower than the EOM-CCSD/cc-pVDZ results and 0.19 eV and 0.18 eV higher than those predicted by CAM-B3LYP-D3(BJ)/cc-pVDZ and ωB97X-D/cc-pVDZ, respectively. The differences in vertical excitation energies among TD-DFT, EOM-CCSD, and CASPT2 arise because single-reference methods lack the static electronic correlation needed for multiconfigurational descriptions, which CASPT2 includes. This missing static correlation becomes more evident in states with multiconfigurational electronic character (*i.e.,* **bd-S$_0$**; see Figure S1 for further discussion), underscoring the importance of using the CASSCF and CASPT2 methods for our photochemical study. The CASSCF and CASPT2 methods classify the $S_0 \rightarrow S_1$ excitation as an $n_N \rightarrow \pi^*_{NN}$ transition; this nature of the transition aligns with the TD-DFT and EOM-CCSD results. Table 1 summarizes these findings.

Table 1. Benchmarked TD-DFT and CASSCF vertical excitation energies.

Method	State	Energy (eV)	Wavelength (nm)	Oscillator strength	Nature
CAM-B3LYP-D3(BJ)/cc-pVDZ	S_1	3.71	334	0.003	$n_N \rightarrow \pi^*_{NN}$
	S_2	4.24	292	0.000	$\pi_{NN} \rightarrow 2p_B$
	S_3	6.31	196	0.000	$n_N \rightarrow \pi^*_{NN}$
ωB97X-D/cc-pVDZ	S_1	3.72	333	0.003	$n_N \rightarrow \pi^*_{NN}$
	S_2	4.29	289	0.000	$\pi_{NN} \rightarrow 2p_B$
	S_3	6.29	197	0.000	$n_N \rightarrow \pi^*_{NN}$
EOM-CCSD/cc-pVDZ	S_1	4.07	305	0.004	$n_N \rightarrow \pi^*_{NN}$
	S_2	4.47	277	0.000	$\pi_{NN} \rightarrow 2p_B$
	S_3	6.58	188	0.000	$n_N \rightarrow \pi^*_{NN}$
SA5-CASSCF(12,11)/cc-pVDZ	S_1	4.50	276	0.010	$n_N \rightarrow \pi^*_{NN}$
	S_2	4.67	265	0.000	$\pi_{NN} \rightarrow 2p_B$
	S_3	6.82	182	0.000	$n_N \rightarrow \pi^*_{NN}$
SA5-CASPT2(12,11)/cc-pVDZ//SA5-CASSCF(12,11)/cc-pVDZ	S_1	3.90	318		$n_N \rightarrow \pi^*_{NN}$
	S_2	4.32	287		$\pi_{NN} \rightarrow 2p_B$
	S_3	5.57	223		$n_N \rightarrow \pi^*_{NN}$

After comparing the orbital transitions, vertical excitation energies, and oscillator strengths across CASSCF(12,11), CASPT2(12,11), TD-DFT, and EOM-CCSD methods, we determined that calculations using CAS(12,11), as illustrated in Figure S1, effectively capture the vertical excitation energies of **bd** at equilibrium (*i.e.,* **bd-S$_0$**). Consequently, we employed SA5-CASSCF(12,11)/cc-pVDZ for all the following calculations.

View Article Online
DOI: 10.1039/D6CP00519E

Predicted absorption spectra and S_1 minimum energy path

To confirm **bd** has an accessible S_0 to S_1 excitation, we calculate its absorption spectrum. We generated 500 Wigner-sampled non-equilibrium geometries based on the ground state frequencies of **bd** (Figure 3a) and calculated the vertical excitation energies [$S_0 \rightarrow S_n$ (n=0-4)] for each structure using MS-CASPT2(12,11)/cc-pVDZ//CAS(12,11)/cc-pVDZ. We consolidate the results of the 500 vertical excitation calculations into the computed spectra shown in Figure 3b.

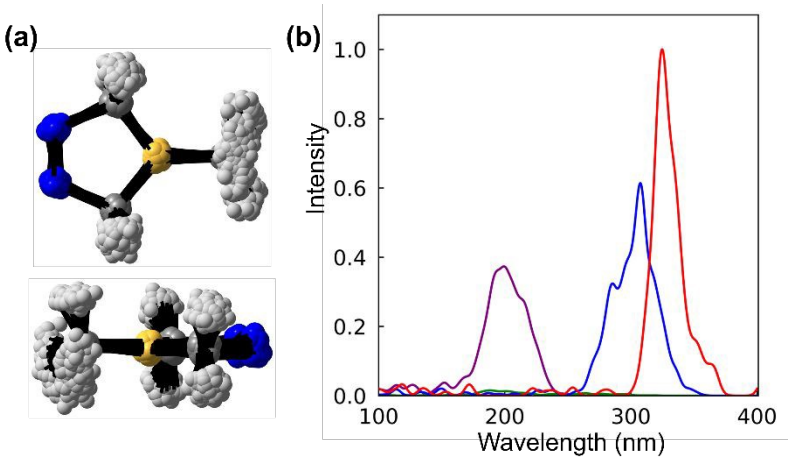

Figure 3. (a) The top view (top) and side view (bottom) overlay of 500 non-equilibrium structures from the Wigner ensemble of **bd**. (b) The predicted absorption spectrum was obtained by averaging the 500 vertical-excitation energy calculations. The absorption intensity is normalized to the peak with the highest oscillator strength, S_1. All calculations utilized the MS-CASPT2(12,11)/cc-pVDZ//CASSCF(12,11)/cc-pVDZ method.

The calculated spectrum exhibits three prominent peaks at 325 nm, 308 nm, and 200 nm, along with a minor peak at 188 nm. The red peak at 325 nm corresponds to the $S_0 \rightarrow S_1$ ($n_N \rightarrow \pi^*_{NN}$) transition and is the most intense, despite being spectroscopically forbidden. The blue peak, centered at 308 nm, corresponds to an $S_0 \rightarrow S_2$ ($n_N \rightarrow 2p_B$) transition; this peak has the second-highest intensity and significant overlap with the $S_0 \rightarrow S_1$ ($n_N \rightarrow \pi^*_{NN}$) peak. The purple peak at 200 nm corresponds to the $S_0 \rightarrow S_4$ ($n_N \rightarrow 2p_B$) transition; it has the lowest intensity of the three major peaks. The green peak at 188 nm corresponds to the $S_0 \rightarrow S_3$ ($n_N \rightarrow \pi^*_{NN}$) transition. Its intensity is minimal compared to the other peaks [*i.e.,* $S_0 \rightarrow S_n$ (n=1, 2, and 4)]; it significantly overlaps with the $S_0 \rightarrow S_4$ peak. Like $S_0 \rightarrow S_1$, the $S_0 \rightarrow S_3$ transition is also spectroscopically forbidden (*i.e.,* $n_N \rightarrow \pi^*_{NN}$). The variation in intensity between the $S_0 \rightarrow S_1$ and $S_0 \rightarrow S_3$ peaks arises from the different n_N orbitals involved in the electronic transitions (*i.e.,* out-of-phase and in-phase n_N orbitals, respectively). The out-of-phase n_N orbital in the $S_0 \rightarrow S_1$ transition shows greater overlap with the π^*_{NN} orbital compared to the in-phase n_N orbital in the $S_0 \rightarrow S_3$ excitation (See Supplementary Figure S3). This leads to the $S_0 \rightarrow S_1$ being the bright state, while the $S_0 \rightarrow S_3$ peak has the lowest intensity of all the peaks. The $S_0 \rightarrow S_1$ ($n_N \rightarrow \pi^*_{NN}$) and $S_0 \rightarrow S_2$ ($n_N \rightarrow 2p_B$) transitions are accessible via a 254 nm ultraviolet light source. In contrast, the $S_0 \rightarrow S_3$ ($n_N \rightarrow \pi^*_{NN}$) and $S_0 \rightarrow S_4$ ($n_N \rightarrow 2p_B$) transitions are inaccessible because the required excitation energy exceeds the energy of the photon source. The overlap and accessibility of $S_0 \rightarrow S_1$ ($n_N \rightarrow \pi^*_{NN}$) and $S_0 \rightarrow S_2$ ($n_N \rightarrow 2p_B$) peaks suggest a role in the photodenitrogenation of **bd**. We will focus on these excitations and their photochemistry.

After assessing the spectral properties, we focused on elucidating the photodenitrogenation mechanism. Since the S_1 state is an accessible bright state, we calculated the minimum energy path (MEP) to find the steepest descent along the S_1 surface, starting from the Franck-Condon point of **bd-S_0**. We hypothesized that the diazo double bond (π_{NN}) will elongate along the S_1-MEP due to $n_N \rightarrow \pi^*_{NN}$ excitation. Figure 4 shows the S_1-MEP, ground state geometry (**bd-S_0**), final MEP geometry (**bd-MEP-8**), and the S_1 minimum (**bd-S_1**).

View Article Online
DOI: 10.1039/D6CP00519E

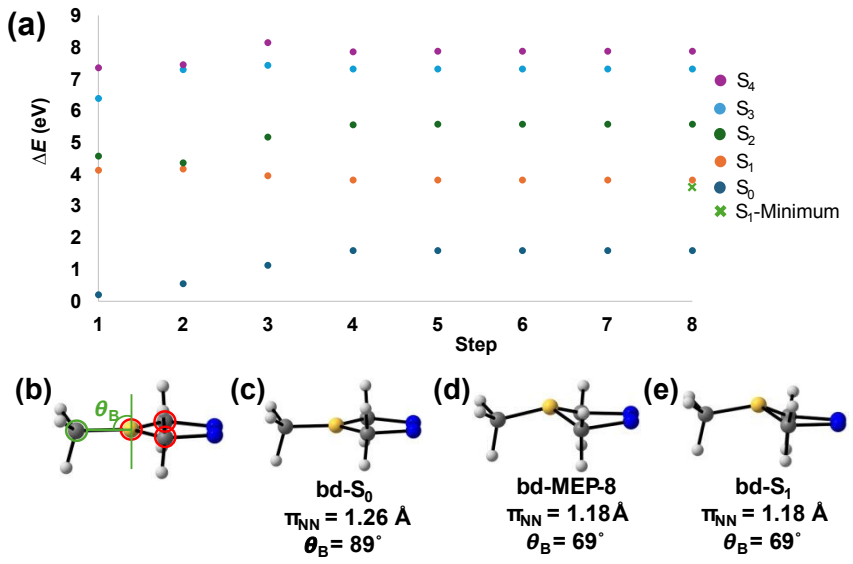

Figure 4. (a) The calculated SA5-CASPT2(12,11)/cc-pVDZ minimum energy path of **bd** along the S_1 surface. (b) The out-of-plane angle θ_B quantifies boron pyramidalization. The plane is defined by C_8-B_3-C_{11} (shown in red), with an orthogonal vector from this plane and the carbon of the methyl group defining the measured angle, θ_{BP} (highlighted in green). (c) The ground state structure, optimized with SA5-CASSCF(12,11)/cc-pVDZ, **bd-S_0**. (d) The final step of the MEP, **bd-MEP-8**, and (e) the optimized S_1 structure, **bd-S_1**. The corresponding diazo double bond length (π_{NN}) and boron pyramidalization (θ_{BP}) values are shown below each structure.

Figure 4 demonstrates the MEP along the S_1 surface and the energies corresponding to the S_0-S_4 states; it includes 8 geometries [**bd-MEP-X** (X=1-8)]. We observe that in the initial two steps of the S_1-MEP (*i.e.,* **bd-MEP-1** and **bd-MEP-2**), the S_1 surface is energetically close to the S_2 surface; the S_2-S_1 energy gaps are 0.46 eV and 0.21 eV, respectively. The small S_2-S_1 energy gaps in **bd-MEP-1** and **bd-MEP-2** suggest a rapid crossing between the S_1 and S_2 surfaces immediately outside the Franck-Condon point. The S_1-MEP converges to a structure, **bd-MEP-8**, 3.83 eV above **bd-S_0**. At **bd-MEP-8**, the S_1-S_0 energy gap is 2.23 eV; this large gap indicates there is no significant coupling between the S_1 and S_0 surfaces (*i.e.,* no S_1/S_0 crossing). Therefore, the steepest descent on the S_1 surface leads toward a radiative decay channel rather than the proposed photodenitrogenation. The two geometries, **bd-S_0** and **bd-MEP-8**, shown in Figures 4c and 4d have π_{NN} bond lengths of 1.26 Å and 1.18 Å, respectively, reflecting a decrease of 0.08 Å from the Franck-Condon geometry to **bd-MEP-8**. Instead of the expected elongation of the π_{NN} bond, we saw boron undergo a conformational change, shifting from a planar conformation in **bd-S_0** (Figure 4d) to a pyramidalized conformation in **bd-MEP-8** (Figure 4e). These structures—**bd-S_0** and **bd-MEP-8**—demonstrate that boron pyramidalization outcompetes the elongation of the π_{NN} bond along the S_1-MEP. We attribute boron pyramidalization to an increase in electron occupancy in the $2p_B$ orbital, along the S_1-MEP, despite the initial $n_N \rightarrow \pi^*_{NN}$ excitation.

To measure the extent of boron pyramidalization, we defined an out-of-plane angle, θ_{BP}, where a planar boron (unoccupied $2p_B$ orbital) has a θ_{BP} of 90˚, and an ideally pyramidalized boron (occupied $2p_B$ orbital) has a θ_{BP} outside of 75°-105° (Figure 4b). **bd-S_0** and **bd-MEP-8** show θ_{BP} values of 89˚ and 69˚, respectively. The 20˚ decrease in θ_{BP} from **bd-S_0** to **bd-MEP-8** indicates a full pyramidalization of the boron along the S_1-MEP. This boron pyramidalization occurs alongside the previously observed 0.08 Å reduction in the π_{NN} bond length. The concurrent shortening of the π_{NN} bond and boron pyramidalization along the S_1 MEP suggests that the $2p_B$ orbital is gaining electron occupancy along the steepest S_1 path. This is supported by the notable overlap of the $S_0 \rightarrow S_1$ ($n_N \rightarrow \pi^*_{NN}$) and $S_0 \rightarrow S_2$ ($n_N \rightarrow 2p_B$) transition peaks observed in the absorption spectra (Figure 3b), suggesting that the $S_0 \rightarrow S_2$ ($n_N \rightarrow 2p_B$) transition is energetically accessible. Additionally, the near-degeneracy of the S_2 and S_1 surfaces along the S_1-MEP (**bd-MEP-2**; Figure 4a) reinforces this conclusion. These findings imply that the photodenitrogenation process involves charge transfer between the π^*_{NN} and $2p_B$ orbitals.

Due to the large S_1/S_0 energy gap at **bd-MEP-8**, we optimized an S_1 minimum, **bd-S_1**, using the last step of the MEP as an initial guess. **bd-S_1** has a π_{NN} of 1.18 Å and θ_{BP} of 69˚; it is 3.61

View Article Online
DOI: 10.1039/D6CP00519E

eV above the **bd-S$_0$**. These values show decreases of 0.08 Å and 20° for π_{NN} and θ_{BP}, respectively, from **bd-S$_0$** to **bd-S$_1$**. These measurements indicate that the boron in **bd-S$_1$** is pyramidalized relative to **bd-S$_0$**. **bd-S$_1$** and **bd-MEP-8** shared π_{NN} and θ_{BP} values (1.18 Å and 69˚, respectively) and had similar energies (3.83 eV and 3.61 eV, respectively), indicating that these structures occupy similar regions of the potential energy surface. At **bd-S$_1$**, a 2.26 eV S_1/S_0 energy gap confirms a nonradiative decay channel via the S_1 MEP, contradicting the hypothesis of nonradiative photodenitrogenation to **5**. Although the S_1-MEP offers detailed insight along the steepest S_1-path, it neglects essential dynamical effects required to study the excited-state mechanism of **bd**.

We accounted for the missing dynamical effects by running quantum-mechanical nonadiabatic molecular dynamics (QM-NAMD) simulations using our open-source Python Rapid *Ab Initio* Artificial Intelligence Molecular Dynamics (PyRAI^{2}MD) software.[22, 23] We generated 700 initial conditions for production trajectories using Wigner sampling based on **bd-S$_0$** frequencies. The fewest-switches surface-hopping (FSSH) algorithm captured nonadiabatic transitions over 1 ps with analytical nonadiabatic coupling vectors. A trajectory was considered complete if denitrogenation and an S_1/S_0 hop occurred, or if it reached 1 ps. The maximum energy drift allowed for these trajectories was 0.05 a.u.; 261 trajectories met this criterion. After 1 ps, 244 (94%) trajectories were on S_0 surface, and 16 (6%) remained on the S_1 state. Of those passing through an S_1/S_0 hop, 218 underwent denitrogenation to **5** (73) or a diradical, **6** (145). The remaining 26 either stayed as reactants (13) or formed diazoborete, **7** (13).

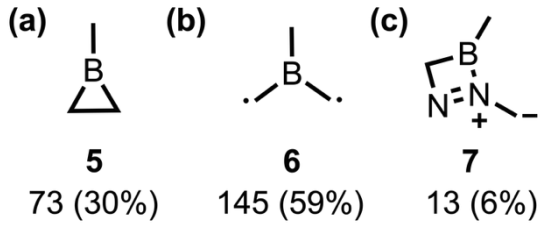

Scheme 2. Product distribution of productive trajectories within our ensemble. The observed products include (a) borirane (**5**), (b) diradical (**6**), and (c) diazoborete (**7**). Below each structure are the number of trajectories leading to each product and their percentages (*i.e.,* quantum yields).

To investigate the photodenitrogenation mechanism, we monitored the two CN bonds (σ_{CN}) that must break for the reaction to proceed throughout our ensemble of trajectories. We propose that denitrogenation may proceed through two possible mechanistic pathways: either both CN bonds break simultaneously (concerted), or one CN bond breaks first, followed shortly by the other (stepwise). We hypothesize that **bd** undergoes stepwise denitrogenation due to increased flexibility from $n_N \rightarrow \pi^*_{NN}$ excitation, enabling π_{NN} rotation (*i.e.,* partial *cis*-to-*trans* isomerization) and σ_{CN} bond cleavage. We plotted the two σ_{CN} bond lengths from 244 trajectories ending in the ground state in Figure 5. Additionally, two arbitrary profiles are shown as dashed lines, representing the ideal stepwise (red) and concerted (gray) denitrogenation pathways within this trajectory map.

View Article Online
DOI: 10.1039/D6CP00519E

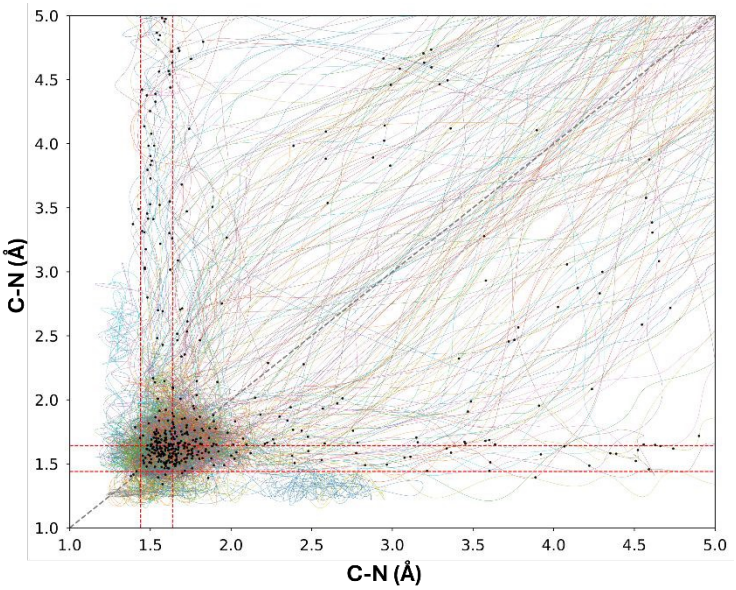

Figure 5. Trajectory map of the photodenitrogenation reaction of **bd**. Each line represents a single trajectory, with black dots marking S_1/S_0 hopping points. We tracked the two CN bonds (σ_{CN}) that must break for photodenitrogenation during the NAMD simulations. To illustrate an ideal stepwise denitrogenation mechanism, we drew an arbitrary bilinear profile with red dashed lines indicating ±0.1 Å around the optimized C-N distance (1.54 Å) in the S_0 state. A trajectory would follow this bilinear profile, with one CN bond elongating while the other stays within the red boundaries. Once the first CN bond breaks, the second CN bond then elongates and breaks as well. To depict an ideal concerted denitrogenation mechanism, we included an arbitrary 1:1 line, indicating that both CN bonds elongate simultaneously until denitrogenation occurs.

In Figure 5, both concerted and stepwise mechanisms are present, indicating that neither pathway dominates; instead, both are readily accessible for the denitrogenation reaction of **bd**. To clearly classify the denitrogenation mechanism in the ensemble of trajectories, we used the literature definition of dynamically stepwise or dynamically concerted mechanism, as reported by Yang *et al*.[92] We determined that of the 244 trajectories that terminate in the S_0 state, 218 undergo denitrogenation. 60 (28%) followed a dynamically stepwise mechanism, while 158 (72%) followed a dynamically concerted mechanism. Thus, denitrogenation of **bd** is mainly driven by the dynamically concerted mechanism.

Having established that the dynamically concerted mechanism (72%) outcompetes the dynamically stepwise mechanism (28%), we now examine the consistent boron pyramidalization in static (**bd-S_1** and **bd-MEP-8)** and dynamic (QM-NAMD) calculations. The pyramidilized boron in these geometries indicates that the $2p_B$ orbital acquires additional electron occupancy along the S_1 surface from the π^*_{NN} (*i.e.,* a charge transfer). We hypothesize that trajectories will adopt one of two geometries (*i.e.,* boron pyramidalization or partial *cis*-to-*trans* π_{NN} isomerization) on the S_1 surface, and those adopting boron pyramidalization will not denitrogenate.

To measure the extent of boron pyramidalization and partial *cis*-to-*trans* π_{NN} isomerization in the denitrogenation mechanism within our trajectory ensemble, we used the geometrical parameters and thresholds presented in Figure 6: θ_{BP} and θ_{CNNC}.

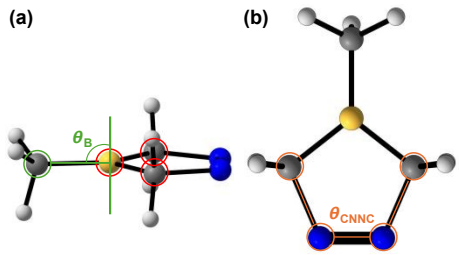

Figure 6. (a) The out-of-plane angle θ_{BP} is defined as the angle between the methyl-boron and the normal vector (green) to the plane formed by the atoms highlighted in red. We defined a planar boron with θ_{BP} values of 75°-105°; otherwise, we classified the boron as pyramidilized. (b) The dihedral angle, θ_{CNNC}, is defined by the C-N-N-C (orange); we classify the *cis*-π_{NN} as having θ_{CNNC} values from -25° to 25°, while other configurations are considered partial *trans*-π_{NN}.

Based on the geometrical descriptions shown in Figure 6, we observed that 177 trajectories (82%) exhibit boron pyramidalization, while 182 (83%) undergo a partial *cis*-to-*trans* π_{NN} isomerization. Out of 218 trajectories that underwent denitrogenation, 120 trajectories included both geometries, 37 only experienced boron pyramidalization, and 59 only experienced partial π_{NN} isomerization. These statistics show that **bd** can undergo denitrogenation via either the boron pyramidalization or the partial π_{NN} isomerization pathway; however, the major pathway includes both.

View Article Online
DOI: 10.1039/D6CP00519E

Out of 120 trajectories that experience both geometries, 12 initially undergo partial π_{NN} isomerization, while 108 first experience boron pyramidalization. The π_{NN} isomerization and boron pyramidalization conformations are linked to the electronic occupancy of the π^*_{NN} orbital and the $2p_B$ orbital, respectively. The frequent occurrence of both geometries is associated with the near degeneracy between the S_1 and S_2 surfaces in the Franck-Condon region, which correspond to the $n_N \rightarrow \pi^*_{NN}$ and $n_N \rightarrow 2p_B$ transitions, respectively. Furthermore, the favorable spatial overlap between the π^*_{NN} and $2p_B$ orbitals facilitates charge transfer, thereby enabling the adoption of the associated conformations (*i.e.,* partial π_{NN} isomerization and boron pyramidalization). Statistically, the photodenitrogenation process begins with boron pyramidalization, followed by partial π_{NN} isomerization, and ends with denitrogenation. We identified a trajectory that proceeds through partial π_{NN} isomerization and boron pyramidalization during denitrogenation, characterized by the angles θ_{CNNC} and θ_{BP}, respectively. Figure 7 provides a detailed analysis of this trajectory.

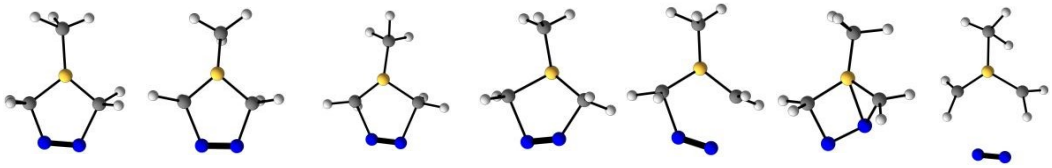

Time (fs)	0	50	400	500	650	858.5	900
θ_{BP}(°)	82	139	140	46	124	71	114
θ_{CNNC}(°)	10	-5	1	-16	-21	57	-8

Figure 7. Snapshots of a representative trajectory that undergoes the denitrogenation on the S_1 surface via the mechanistic pathway that includes boron pyramidalization and partial *cis*-to-*trans* π_{NN} isomerization.

Figure 7 shows snapshots of a trajectory undergoing denitrogenation via the dominant pathway that involves the partial π_{NN} isomerization and boron pyramidalization. At 0 fs, θ_{BP} is 82°, and θ_{CNNC} is 10°. At 50 fs, θ_{BP} is 139°, and θ_{CNNC} is -5°. By 400 fs, θ_{BP} and θ_{CNNC} are 140° and 1°, respectively. At 500, θ_{BP} is 46°, and θ_{CNNC} is -16°. At 650 fs, θ_{BP} is 124°, and θ_{CNNC} is -21°. By 858.5 fs, θ_{BP} is 71°, and θ_{CNNC} is 57°. At 900 fs, θ_{BP} is 114°, and θ_{CNNC} is -8°. Between 0 fs and 50 fs, θ_{BP} and θ_{CNNC} increased by 57° and 15°, respectively. The rapid rise in θ_{BP} (57°) with a small decrease in θ_{CNNC} (15°) suggests the $2p_B$ orbital gains electron occupancy, driving the mechanism, rather than the π^*_{NN} orbital. In the next 350 fs (50 fs to 400 fs), θ_{BP} and θ_{CNNC} increased by 1° and 6°, respectively, demonstrating that the geometry remains unchanged. We attribute this persistent geometry to the close resemblance between the 50-fs geometry and **bd-S$_1$**. From 400 fs to 500 fs, θ_{BP} decreased by 94°, and θ_{CNNC} increased by 17°. The decrease in θ_{BP} from 140° to 46° indicates that the trajectory rehybridizes boron from sp^2 to sp^3, in the opposite direction to the initial pyramidalization. By 650 fs, θ_{BP} increased by 78°, and θ_{CNNC} decreased by 5°. Like the previous 100-fs window, the changes in θ_{BP} and θ_{CNNC} for the 500 fs to 650 fs period suggest that the sp^3 boron has inverted, while the π_{NN} bond remains in the *cis*-configuration. The fluctuation in the θ_{BP} indicates prolonged occupation of the $2p_B$ orbital, whereas minimal changes in θ_{CNNC} suggest that the π^*_{NN} orbital remains empty during this period. Within the 650-fs to 858.5-fs time window, the θ_{BP} decreased by 53°, and θ_{CNNC} increased by 78°; at the 858.5-fs geometry, the trajectory underwent an S_1/S_0 hop. The lower θ_{BP} value (71°) is 4° below our planar boron threshold (75°), while the higher θ_{CNNC} (57°) indicates a partial *cis*-to-*trans* π_{NN} isomerization. These geometric changes show that the $2p_B$ orbital is essentially empty, while the π^*_{NN} orbital is occupied. 41.5 fs (*i.e.,* at 900 fs) after the S_1/S_0 hop, the trajectory denitrogenates towards the 1,3-diyl. This trajectory shows the mechanistic pathway involving boron pyramidalization and partial π_{NN} isomerization. Boron pyramidalization occurs first, followed by partial π_{NN} isomerization, which leads to denitrogenation. Minor denitrogenation pathways are explored in Figures S4 and S5.

View Article Online
DOI: 10.1039/D6CP00519E

Minor pathways

After analyzing the mechanisms for the major product, we investigate the pathway to the minor product, diazoborete (**7**). We identified a trajectory bypassing denitrogenation, leading to **7**. To compare with earlier figures, we measured θ_{BP} and θ_{CNNC} along this trajectory. Thirteen trajectories (6%) showed this rearrangement. Figure 8 examines a representative trajectory in detail.

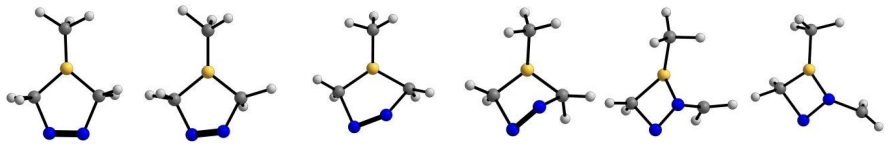

Time (fs)	0	50	100	130	150	200
θ_{BP}(°)	90	83	84	96	93	53
θ_{CNNC}(°)	-10	-54	-35	-70	-92	-150

Figure 8. Snapshots of a representative trajectory that does not involve denitrogenation on the S_1 surface; instead, it involves an insertion-like reaction that results in BN bond formation and BC bond cleavage, producing diazoborete (**7**).

Figure 8 provides snapshots of the representative trajectory. θ_{BP} and θ_{CNNC} are reported to facilitate direct comparison with previous figures (Figures 7 and S4-5). At 0 fs, θ_{BP} measures 90° while θ_{CNNC} is -10°. By 50 fs, θ_{BP} is 83°, whereas θ_{CNNC} measures -54°. At 100 fs, θ_{BP} is 84°, with θ_{CNNC} equal to -35°. By 130 fs, θ_{BP} reaches 96°, and θ_{CNNC} is -70°. At 150 fs, θ_{BP} measures 93°, while θ_{CNNC} is at -92°. Finally, at 200 fs, θ_{BP} measures 53°, and θ_{CNNC} is -150°. Between 0 fs and 50 fs, θ_{BP} drops by 7°, and θ_{CNNC} decreases by 44°. This suggests that the $2p_B$ orbital remains unoccupied during this period, while the π^*_{NN} orbital gains electron occupancy. In the following 50 fs (50 fs to 100 fs), θ_{BP} and θ_{CNNC} increased by 1° and decreased by 19°, respectively, indicating a prolonged occupancy of the π^*_{NN} orbital. From 100 fs to 130 fs, there is a 12° increase in θ_{BP} and a 35° decrease in θ_{CNNC}. Although the θ_{BP} increase is significant, boron remains in a planar conformation, not pyramidalizing per our geometric thresholds. At the 130-fs geometry, the trajectory undergoes an S_1/S_0 hop. Between 130 fs and 150 fs, the θ_{BP} decreases by 3°, while θ_{CNNC} decreases by 22°. Due to partial π_{NN} isomerization, the n_N orbital aligns with the $2p_B$ orbital, leading to BN bond formation and BC bond cleavage; this rearrangement results in **7**. Between 150 fs and 200 fs, the θ_{BP} drops by 40°, and θ_{CNNC} decreases by 58°. At this stage, the reference plane for θ_{BP} and the dihedral θ_{CNNC} have increased conformational freedom due to the rearrangement, rendering both measurements geometrically meaningless. This structure remains in the ground state and undergoes further rearrangements, as shown in Supplementary Figure S3.

Conclusion

This study provides a complete enumeration of the mechanistic pathways for the photochemical denitrogenation of 1-methylborodiazene (**bd**) towards base-free 1-methylborirane (**5**). We employed static multiconfigurational quantum-mechanical computations, combined with quantum–mechanical nonadiabatic molecular dynamics (QM-NAMD), to provide mechanistic insights from static and dynamic perspectives. Our static minimum-energy path calculation showed the formation of a pyramidalized structure (**bd-MEP-8**) relative to the optimized S_0-state geometry (**bd-S_0**) along the steepest S_1-path. We optimized **bd-MEP-8** to an S_1-minimum with pyramidalized boron (**bd-S_1**). Static calculations indicate that the steepest-descent path on the S_1 surface leads to fluorescence decay rather than to the photochemical denitrogenation. Static calculations, although informative, miss critical dynamical effects. As such, we used our open-source software, PyRAI^{2}MD, to perform QM-NAMD. Our QM-NAMD trajectories show that the denitrogenation reaction mainly follows a dynamically concerted mechanism (72%), involving two key geometries: partial π_{NN} isomerization and boron pyramidalization. Of 218 trajectories, 120

View Article Online
DOI: 10.1039/D6CP00519E

(55%) involved both, 37 (17%) had only boron pyramidalization, and 59 (27%) only partial *cis*-to-*trans* π_{NN} isomerization. As such, we concluded that denitrogenation can occur through either the boron pyramidalization pathway or the partial π_{NN} isomerization path, but the dominant pathway involves both geometries. We attribute the high prevalence of these geometries to the near-degeneracy between S_2- and S_1-states near the Franck-Condon region. The $S_0 \rightarrow S_1(n_N \rightarrow \pi^*_{NN})$ and $S_0 \rightarrow S_2(n_N \rightarrow 2p_B)$ transitions cause **bd** to undergo conformational changes, such as partial π_{NN} isomerization or boron pyramidalization, thereby facilitating denitrogenation. Most trajectories (71%) experience denitrogenation on the S_0 surface, while a smaller portion (29%) fully denitrogenates on the S_1 surface. We predicted quantum yields of 21% for **5** and 67% for **6**.

Conflicts of interest

There are no conflicts of interest to declare.

Acknowledgements

The National Science Foundation Center under NSF-CHE-2144556 supported this work. We appreciate the assistance from the Northeastern Research Computing Team and the computing resources provided by the Massachusetts Life Science Center grant (G00006360). We dedicate this manuscript to Professor David Yarkony, who contributed 47 years to advancing theoretical chemistry and was very supportive of our research.

Computational Methods

Single Reference methods

For all our density-based electronic structure methods (*i.e.,* DFT and TD-DFT), we used Gaussian 16.B01.[93] We used DFT to optimize the initial ground-state global minimum of **bd** using the PBE0/cc-pVDZ method. We used time-dependent density functional theory (TD-DFT) to calculate the vertical excitation energies of **bd** using the CAM-B3LYP-GD3(BJ) and ωB97X-D functionals with the cc-pVDZ basis set. We used Gaussian 16.B01[93] to run the equation of motion coupled-cluster single doubles (EOM-CCSD) with the cc-pVDZ basis set.

Multiconfigurational methods

We employed the state-average complete active space self-consistent field (SA-CASSCF) method, as implemented in OpenMolcas 19.11.[94] This approach uses the format SA(N)-CASSCF(*m*,*n*), where N denotes the number of singlet states averaged in the calculation, while *m* and *n* denote the number of electrons and orbitals in the active space. Implementing the CASSCF method poses challenges, including appropriate active space selection and the inherent computational expense. The size of the active space is intrinsically connected to computational cost, scaling O(C(2n,m)) where n is the number of orbitals and m is the number of electrons.[95] To the best of our knowledge, the current maximum active space size in contemporary computing hardware is 18 electrons distributed across 18 orbitals in OpenMolcas[94] and NWChem[96, 97].

Quantum Mechanical Nonadiabatic Molecular Dynamics

To incorporate the missing dynamical effects from previous static calculations—such as vertical excitation energies, computed absorption spectra, and the minimum energy path—we performed quantum mechanical nonadiabatic molecular dynamics (QM-NAMD) simulations. We generated 700 initial conditions for production trajectories using Wigner sampling based on **bd-S_0** frequencies. All computations were performed using OpenMolcas 19.11[94] through our open-source software, PyRAI^{2}MD.[22, 23] Trajectory propagation employed our SA5-CASSCF(12,11)/cc-pVDZ electronic-structure method with the Verlet algorithm, using a 0.5 fs time step. The fewest-switches surface-hopping (FSSH) algorithm tracked nonadiabatic transitions over 1 ps, utilizing analytical nonadiabatic coupling vectors. All trajectories were launched from the S_1 surface; a trajectory was deemed complete if denitrogenation and an S_1/S_0 hop occurred, or if it reached 1 ps. Trajectories that had a maximal energy drift exceeding 0.05 a.u. were eliminated from the analysis. In total, 261 trajectories satisfied these criteria.

References

View Article Online
DOI: 10.1039/D6CP00519E

(1) Cho, S.; Usuba, J.; Chakraborty, S.; Li, X.; Han, G. G. D. Solid-state photon energy storage via reversible [2+2] cycloaddition of donor-acceptor styrylpyrylium system. *Chem* **2023**. DOI: 10.1016/j.chempr.2023.06.007.
(2) Skolia, E.; Kokotos, C. G. Photochemical [2 + 2] Cycloaddition of Alkenes with Maleimides: Highlighting the Differences between N-Alkyl vs N-Aryl Maleimides. *ACS Org Inorg Au* **2023**, *3* (2), 96-103. DOI: 10.1021/acsorginorgau.2c00053.
(3) Paderes, M. C.; Jeffrey Diaz, M.; Pagtalunan, C. A.; Bruzon, D. A.; Tapang, G. A. Photo-Controlled [4+4] Cycloaddition of Anthryl-Polymer Systems: A Versatile Approach to Fabricate Functional Materials. *Chem Asian J* **2022**, *17* (12), e202200193. DOI: 10.1002/asia.202200193.
(4) Mukadum, F.; Nguyen, Q.; Adrion, D. M.; Appleby, G.; Chen, R.; Dang, H.; Chang, R.; Garnett, R.; Lopez, S. A. Efficient Discovery of Visible Light-Activated Azoarene Photoswitches with Long Half-Lives Using Active Search. *J Chem Inf Model* **2021**, *61* (11), 5524-5534. DOI: 10.1021/acs.jcim.1c00954.
(5) Li, X.; Cho, S.; Wan, J.; Han, G. G. D. Photoswitches and photochemical reactions for optically controlled phase transition and energy storage. *Chem* **2023**, *9* (9), 2378-2389. DOI: 10.1016/j.chempr.2023.05.029.
(6) Lee, H.; Tessarolo, J.; Langbehn, D.; Baksi, A.; Herges, R.; Clever, G. H. Light-Powered Dissipative Assembly of Diazocine Coordination Cages. *Journal of the American Chemical Society* **2022**, *144* (7), 3099-3105. DOI: 10.1021/jacs.1c12011.
(7) Adrion, D. M.; Karunaratne, W. V.; Lopez, S. A. Multiconfigurational photodynamics simulations reveal the mechanism of photodecarbonylations of cyclopropenones in explicit aqueous environments. *Chem Sci* **2023**, *14* (45), 13205-13218. DOI: 10.1039/d3sc03805j.
(8) Shields, D. J.; Karothu, D. P.; Sambath, K.; Ranaweera, R.; Schramm, S.; Duncan, A.; Duncan, B.; Krause, J. A.; Gudmundsdottir, A. D.; Naumov, P. Cracking under Internal Pressure: Photodynamic Behavior of Vinyl Azide Crystals through N(2) Release. *J Am Chem Soc* **2020**, *142* (43), 18565-18575. DOI: 10.1021/jacs.0c07830.
(9) Datta, S.; Davis, H. F. Photodissociation Dynamics of the Simplest Diazirine: Cyclo-CH(2)N(2) --> CH(2) + N(2). *J Phys Chem A* **2025**, *129* (15), 3498-3507. DOI: 10.1021/acs.jpca.5c00801.
(10) Hui, C.; Wang, S.; Xu, C. Dinitrogen extrusion from diazene in organic synthesis. *Chinese Chemical Letters* **2022**, *33* (8), 3695-3700. DOI: 10.1016/j.cclet.2022.03.073.
(11) Chang, T. Y.; Adrion, D. M.; Meyer, A. R.; Lopez, S. A.; Garcia-Garibay, M. A. A Green Chemistry Approach toward the Stereospecific Synthesis of Densely Functionalized Cyclopropanes via the Solid-State Photodenitrogenation of Crystalline 1-Pyrazolines. *J Org Chem* **2022**, *87* (5), 2277-2288. DOI: 10.1021/acs.joc.1c01808.
(12) Zhu, S.; Jia, L.; Cheng, Q.; Sun, Q.; Chen, X.; Yu, H.; Han, Y.; Hou, H. Visible-Light-Induced Stereoselective Radical trans-Iodoalkylation of Terminal Alkyne with Iodoform. *Org Lett* **2024**, *26* (39), 8400-8404. DOI: 10.1021/acs.orglett.4c03241.
(13) Pierau, L.; Versace, D. L. Light and Hydrogels: A New Generation of Antimicrobial Materials. *Materials (Basel)* **2021**, *14* (4). DOI: 10.3390/ma14040787.
(14) López-Cano, M.; Scortichini, M.; Tosh, D. K.; Salmaso, V.; Ko, T.; Salort, G.; Filgaira, I.; Soler, C.; Trauner, D.; Hernando, J.; et al. Photoswitchable Diazocine Derivative for Adenosine A3 Receptor Activation in Psoriasis. *Journal of the American Chemical Society* **2025**, *147* (1), 874-879. DOI: 10.1021/jacs.4c13558.
(15) Homan, R. A.; Lapek, J. D.; Woo, C. M.; Niessen, S.; Jones, L. H.; Parker, C. G. Photoaffinity labelling with small molecules. *Nature Reviews Methods Primers* **2024**, *4* (1). DOI: 10.1038/s43586-024-00308-4.
(16) Hernandez, F. J.; Cox, J. M.; Li, J.; Crespo-Otero, R.; Lopez, S. A. Multiconfigurational Calculations and Photodynamics Describe Norbornadiene Photochemistry. *J Org Chem* **2023**, *88* (9), 5311-5320. DOI: 10.1021/acs.joc.2c02758.

View Article Online
DOI: 10.1039/D6CP00519E

(17) Scott, P. J.; Kasprzak, C. R.; Feller, K. D.; Meenakshisundaram, V.; Williams, C. B.; Long, T. E. Light and latex: advances in the photochemistry of polymer colloids. *Polymer Chemistry* **2020**, *11* (21), 3498-3524. DOI: 10.1039/d0py00349b.
(18) Xu, T. Y.; Tong, F.; Xu, H.; Wang, M. Q.; Tian, H.; Qu, D. H. Engineering Photomechanical Molecular Crystals to Achieve Extraordinary Expansion Based on Solid-State [2 + 2] Photocycloaddition. *J Am Chem Soc* **2022**, *144* (14), 6278-6290. DOI: 10.1021/jacs.1c12485.
(19) Gatlin, D. M.; Karney, W. L.; Abe, M.; Ault, B. S.; Gudmundsdottir, A. D. Formation and Reactivity of Triplet Vinylnitrenes as a Function of Ring Size. *J Org Chem* **2019**, *84* (14), 9215-9225. DOI: 10.1021/acs.joc.9b01191.
(20) Ondrus, A. E.; Zhang, T. Structure, Bonding, and Photoaffinity Labeling Applications of Dialkyldiazirines. *Synlett* **2021**, *32* (11), 1053-1059. DOI: 10.1055/a-1437-8202.
(21) Poloukhtine, A. A.; Mbua, N. E.; Wolfert, M. A.; Boons, G.-J.; Popik, V. V. Selective Labeling of Living Cells by a Photo-Triggered Click Reaction. *Journal of the American Chemical Society* **2009**, *131* (43), 15769-15776. DOI: 10.1021/ja9054096.
(22) Kobatake, S.; Kitagawa, D. Photoresponsive Molecular Crystals for Light-Driven Photoactuators. In *Photosynergetic Responses in Molecules and Molecular Aggregates*, Miyasaka, H., Matsuda, K., Abe, J., Kawai, T. Eds.; Springer Singapore, 2020; pp 427-447.
(23) Luque, A.; Paternoga, J.; Opatz, T. Strain Release Chemistry of Photogenerated Small-Ring Intermediates. *Chemistry* **2021**, *27* (14), 4500-4516. DOI: 10.1002/chem.202004178.
(24) Glarner, F.; Thornton, S. R.; Schärer, D.; Bernardinelli, G.; Burger, U. 6-Azabicyclo[3.1.0]hex-30-en-2-ol Derivative, photochemically generated building blocks for bicyclic β-lactams. *Helvetica Chimica Acta* **1997**, *80* (1), 121-127. DOI: https://doi.org/10.1002/hlca.19970800112 (acccessed 2025/07/11).
(25) Jira, T.; Janos, J.; Slavicek, P. Sensitivity Analysis in Photodynamics: How Does the Electronic Structure Control cis-Stilbene Photodynamics? *J Chem Theory Comput* **2024**, *20* (24), 10972-10985. DOI: 10.1021/acs.jctc.4c01008.
(26) Cox, J. M.; Bain, M.; Kellogg, M.; Bradforth, S. E.; Lopez, S. A. Role of the Perfluoro Effect in the Selective Photochemical Isomerization of Hexafluorobenzene. *J Am Chem Soc* **2021**, *143* (18), 7002-7012. DOI: 10.1021/jacs.1c01506.
(27) Ueda, M.; Jorner, K.; Sung, Y. M.; Mori, T.; Xiao, Q.; Kim, D.; Ottosson, H.; Aida, T.; Itoh, Y. Energetics of Baird aromaticity supported by inversion of photoexcited chiral [4n]annulene derivatives. *Nature Communications* **2017**, *8* (1), 346. DOI: 10.1038/s41467-017-00382-1.
(28) Yan, J.; Slanina, T.; Bergman, J.; Ottosson, H. Photochemistry Driven by Excited-State Aromaticity Gain or Antiaromaticity Relief. *Chemistry* **2023**, *29* (19), e202203748. DOI: 10.1002/chem.202203748.
(29) Hemauer, F.; Steinruck, H. P.; Papp, C. The Norbornadiene/Quadricyclane Pair as Molecular Solar Thermal Energy Storage System: Surface Science Investigations. *Chemphyschem* **2024**, *25* (9), e202300806. DOI: 10.1002/cphc.202300806.
(30) Salkho, N. M.; Awad, N. S.; Pitt, W. G.; Husseini, G. A. Photo-Induced Drug Release from Polymeric Micelles and Liposomes: Phototriggering Mechanisms in Drug Delivery Systems. *Polymers (Basel)* **2022**, *14* (7). DOI: 10.3390/polym14071286.
(31) Sana, B.; Finne-Wistrand, A.; Pappalardo, D. Recent development in near infrared light-responsive polymeric materials for smart drug-delivery systems. *Materials Today Chemistry* **2022**, *25*. DOI: 10.1016/j.mtchem.2022.100963.
(32) Choi, S. K.; Verma, M.; Silpe, J.; Moody, R. E.; Tang, K.; Hanson, J. J.; Baker, J. R., Jr. A photochemical approach for controlled drug release in targeted drug delivery. *Bioorg Med Chem* **2012**, *20* (3), 1281-1290. DOI: 10.1016/j.bmc.2011.12.020.
(33) Petti, A.; Karrasch, M. J.; Chahar, P.; Wessels, F. H.; Holter, N.; Boser, F.; Daniliuc, C. G.; Glorius, F. Cyclic Bifunctional Reagents Enabling a Strain-Release-Driven Formal [3 + 2] Cycloaddition of 2H-Azirines by Cascade Energy Transfer. *J Am Chem Soc* **2025**, *147* (16), 13276-13285. DOI: 10.1021/jacs.4c18080.

View Article Online
DOI: 10.1039/D6CP00519E

(34) Rauscher, N.; Naesborg, L.; Jandl, C.; Bach, T. Concise Total Synthesis of Agarozizanol B via a Strained Photocascade Intermediate. *Angew Chem Int Ed Engl* **2021**, *60* (45), 24039-24042. DOI: 10.1002/anie.202110009.
(35) Huang, J.; You, S. Y.; Hu, L. Z.; He, Y. H.; Guan, Z. One-Pot Photocascade Catalysis: Access to Pyrrole Derivatives from N-Arylglycines and Morita-Baylis-Hillman (MBH) Acetates. *Org Lett* **2024**, *26* (47), 10195-10200. DOI: 10.1021/acs.orglett.4c04176.
(36) Maag, H.; Lemcke, D. J.; Wahl, J. M. Ring opening of photogenerated azetidinols as a strategy for the synthesis of aminodioxolanes. *Beilstein J Org Chem* **2024**, *20*, 1671-1676. DOI: 10.3762/bjoc.20.148.
(37) Luque, A.; Gross, J.; Zahringer, T. J. B.; Kerzig, C.; Opatz, T. Vinylcyclopropane [3+2] Cycloaddition with Acetylenic Sulfones Based on Visible Light Photocatalysis. *Chemistry* **2022**, *28* (18), e202104329. DOI: 10.1002/chem.202104329.
(38) Laktsevich-Iskryk, M.; Hurski, A.; Oseka, M.; Kananovich, D. Recent advances in asymmetric synthesis via cyclopropanol intermediates. *Org Biomol Chem* **2025**, *23* (5), 992-1015. DOI: 10.1039/d4ob01746c.
(39) Mishra, D. R.; Mishra, N. P. Recent breakthroughs in ring-opening annulation reactions of aziridines. *Org Biomol Chem* **2025**, *23* (13), 2967-2996. DOI: 10.1039/d4ob01577k.
(40) Vilotijevic, I.; Jamison, T. F. Epoxide-opening cascades in the synthesis of polycyclic polyether natural products. *Angew Chem Int Ed Engl* **2009**, *48* (29), 5250-5281. DOI: 10.1002/anie.200900600.
(41) Palani, V.; Wendlandt, A. E. Strain-Inducing Positional Alkene Isomerization. *J Am Chem Soc* **2023**, *145* (36), 20053-20061. DOI: 10.1021/jacs.3c06935.
(42) Ma, S.; Mandalapu, D.; Wang, S.; Zhang, Q. Biosynthesis of cyclopropane in natural products. *Nat Prod Rep* **2022**, *39* (5), 926-945. DOI: 10.1039/d1np00065a.
(43) Ju, X.; Lee, M.; Leung, J. C.; Lee, J. Synthesis and Functionalization of Aziridines: A Perspective View from Pharmaceutical Industries. *European Journal of Organic Chemistry* **2025**, *28* (15). DOI: 10.1002/ejoc.202401414.
(44) Hanif, M.; Zahoor, A. F.; Saif, M. J.; Nazeer, U.; Ali, K. G.; Parveen, B.; Mansha, A.; Chaudhry, A. R.; Irfan, A. Exploring the synthetic potential of epoxide ring opening reactions toward the synthesis of alkaloids and terpenoids: a review. *RSC Adv* **2024**, *14* (19), 13100-13128. DOI: 10.1039/d4ra01834f.
(45) Herzberger, J.; Niederer, K.; Pohlit, H.; Seiwert, J.; Worm, M.; Wurm, F. R.; Frey, H. Polymerization of Ethylene Oxide, Propylene Oxide, and Other Alkylene Oxides: Synthesis, Novel Polymer Architectures, and Bioconjugation. *Chem Rev* **2016**, *116* (4), 2170-2243. DOI: 10.1021/acs.chemrev.5b00441.
(46) Uthumange, S. S.; Liew, A. J. H.; Chee, X. W.; Yeong, K. Y. Ringing medicinal chemistry: The importance of 3-membered rings in drug discovery. *Bioorg Med Chem* **2024**, *116*, 117980. DOI: 10.1016/j.bmc.2024.117980.
(47) Wang, N.; Zhao, J.-X.; Yue, J.-M. Total synthesis of cyclopropane-containing natural products: recent progress (2016–2024). *Organic Chemistry Frontiers* **2025**, *12* (7), 2439-2456. DOI: 10.1039/d4qo02316a.
(48) Marco-Contelles, J.; Molina, M. T.; Anjum, S. Naturally Occurring Cyclohexane Epoxides: Sources, Biological Activities, and Synthesis. *Chemical Reviews* **2004**, *104* (6), 2857-2900. DOI: 10.1021/cr980013j.
(49) Maurer, S. J.; Petrarca de Albuquerque, J. L.; McCallum, M. E. Recent Developments in the Biosynthesis of Aziridines. *Chembiochem* **2024**, *25* (16), e202400295. DOI: 10.1002/cbic.202400295.
(50) Thibodeaux, C. J.; Chang, W. C.; Liu, H. W. Enzymatic chemistry of cyclopropane, epoxide, and aziridine biosynthesis. *Chem Rev* **2012**, *112* (3), 1681-1709. DOI: 10.1021/cr200073d.

View Article Online
DOI: 10.1039/D6CP00519E

(51) Wang, H.; Huangfu, S.; Wei, D.; Sun, Z.; Wu, Y.; Yu, X.; Jiang, B.; Chen, H. Triptolide-based cleavable antibody-drug conjugates for pancreatic cancer. *Eur J Med Chem* **2025**, *295*, 117798. DOI: 10.1016/j.ejmech.2025.117798.
(52) Herraiz, A. G.; Suero, M. G. New Alkene Cyclopropanation Reactions Enabled by Photoredox Catalysis via Radical Carbenoids. *Synthesis* **2019**, *51* (14), 2821-2828. DOI: 10.1055/s-0037-1611872.
(53) Han, X.; Zhang, N.; Li, Q.; Zhang, Y.; Das, S. The efficient synthesis of three-membered rings via photo- and electrochemical strategies. *Chem Sci* **2024**, *15* (34), 13576-13604. DOI: 10.1039/d4sc02512a.
(54) Simmons, H. E.; Smith, R. D. A NEW SYNTHESIS OF CYCLOPROPANES FROM OLEFINS. *Journal of the American Chemical Society* **1958**, *80* (19), 5323-5324. DOI: 10.1021/ja01552a080.
(55) Xu, J.; Li, X.; Chen, N. An Improved and Mild Wenker Synthesis of Aziridines. *Synthesis* **2010**, *2010* (20), 3423-3428. DOI: 10.1055/s-0030-1257913.
(56) Wenker, H. The Preparation of Ethylene Imine from Monoethanolamine. *Journal of the American Chemical Society* **1935**, *57* (11), 2328-2328. DOI: 10.1021/ja01314a504.
(57) Thakur, V. V.; Sudalai, A. N-Bromoamides as versatile catalysts for aziridination of olefins using chloramine-T. *Tetrahedron Letters* **2003**, *44* (5), 989-992. DOI: https://doi.org/10.1016/S0040-4039(02)02729-6.
(58) He, Q.; Pu, M. P.; Jiang, Z.; Wang, H.; Feng, X.; Liu, X. Asymmetric Epoxidation of Alkenes Catalyzed by a Cobalt Complex. *J Am Chem Soc* **2023**, *145* (28), 15611-15618. DOI: 10.1021/jacs.3c05476.
(59) Steudel, Y.; Steudel, R.; Wong, M. W. The thermal decomposition of thiirane: a mechanistic study by ab initio MO theory. *Chemistry* **2002**, *8* (1), 217-228. DOI: 10.1002/1521-3765(20020104)8:1<217::aid-chem217>3.0.co;2-0.
(60) Kudo, H.; Naritomi, K.; Onishi, S.; Maekawa, H.; Mondarte, E. A. Q.; Suthiwanich, K.; Hayashi, T. Living Ring-Expansion Polymerization of Thiirane with Cyclic Monocarbamothioates. *Macromolecules* **2020**, *53* (12), 4733-4740. DOI: 10.1021/acs.macromol.0c00687.
(61) Song, S. M.; Jin, J.; Choi, J. H.; Chung, W. J. Synthesis of cis-thiiranes as diastereoselective access to epoxide congeners via 4pi-electrocyclization of thiocarbonyl ylides. *Nat Commun* **2022**, *13* (1), 4818. DOI: 10.1038/s41467-022-32499-3.
(62) Ghosh, A.; Van Nguyen, T. H.; Bellanger, C.; Chelli, S.; Ahmad, M.; Saffon-Merceron, N.; Taillier, C.; Dalla, V.; Mayer, R. J.; Dixon, I. M.; et al. Unraveling C-Selective Ring-Opening of Phosphiranes with Carboxylic Acids and Other Nucleophiles: A Mechanistically-Driven Approach. *Angew Chem Int Ed Engl* **2025**, *64* (2), e202414172. DOI: 10.1002/anie.202414172.
(63) Xin, T.; Geeson, M. B.; Zhu, H.; Qu, Z. W.; Grimme, S.; Cummins, C. C. Synthesis of phosphiranes via organoiron-catalyzed phosphinidene transfer to electron-deficient olefins. *Chem Sci* **2022**, *13* (43), 12696-12702. DOI: 10.1039/d2sc05011k.
(64) Li, X.; Robinson, K. D.; Gaspar, P. P. A New Stereoselective Synthesis of Phosphiranes. *The Journal of Organic Chemistry* **1996**, *61* (22), 7702-7710. DOI: 10.1021/jo9608533.
(65) Herz, F. A. D.; Nobis, M.; Wendel, D.; Pahl, P.; Altmann, P. J.; Tillmann, J.; Weidner, R.; Inoue, S.; Rieger, B. Application of multifunctional silylenes and siliranes as universal crosslinkers for metal-free curing of silicones. *Green Chemistry* **2020**, *22* (14), 4489-4497. DOI: 10.1039/d0gc00272k.
(66) Pan, Y.; Morisako, S.; Aoyagi, S.; Sasamori, T. Generation of Bis(ferrocenyl)silylenes from Siliranes. *Molecules* **2020**, *25* (24). DOI: 10.3390/molecules25245917.
(67) Palmer, W. S.; Woerpel, K. A. Stereospecific Palladium-Catalyzed Reactions of Siliranes with Alkynes. *Organometallics* **1997**, *16* (6), 1097-1099. DOI: 10.1021/om960923w.
(68) Dong, J.; Xu, J. Facile synthesis of thietanes via ring expansion of thiiranes. *Org Biomol Chem* **2017**, *15* (4), 836-844. DOI: 10.1039/c6ob02387h.

View Article Online
DOI: 10.1039/D6CP00519E

(69) Banert, K.; Chityala, M.; Korb, M. Ring Enlargement of Three-Membered Heterocycles by Treatment with In Situ Formed Tricyanomethane. *Chemistry* **2020**, *26* (28), 6158-6164. DOI: 10.1002/chem.202000089.
(70) Kim, H. I.; Veeramanoharan, A.; Selvaraj, B.; Olivier, M.; Lee, E.; Lee, J. W.; Park, C. M. Thiiranes: Intelligent Molecules for S-Persulfidation. *J Am Chem Soc* **2024**, *146* (13), 8820-8825. DOI: 10.1021/jacs.3c12908.
(71) Krasowska, M.; Bettinger, H. F. Computational Study of the Isomerization Reactions of Borirane. *J Org Chem* **2018**, *83* (4), 1804-1809. DOI: 10.1021/acs.joc.7b02715.
(72) Wang, J.; Ye, Q. Borirenes and Boriranes: Development and Perspectives. *Chemistry* **2024**, *30* (11), e202303695. DOI: 10.1002/chem.202303695.
(73) Klusik, H.; Berndt, A. A Boron-Carbon Double Bond. *Angewandte Chemie International Edition in English* **1983**, *22* (11), 877-878. DOI: 10.1002/anie.198308771.
(74) Dzhemilev, U. M.; Khusainova, L. I.; Ryazanov, K. S.; Khafizova, L. O. Boron-containing small rings: synthesis, properties, and application prospects. *Russian Chemical Bulletin* **2021**, *70* (10), 1851-1892. DOI: 10.1007/s11172-021-3292-2.
(75) McFadden, T. R.; Fang, C.; Geib, S. J.; Merling, E.; Liu, P.; Curran, D. P. Synthesis of Boriranes by Double Hydroboration Reactions of N-Heterocyclic Carbene Boranes and Dimethyl Acetylenedicarboxylate. *J Am Chem Soc* **2017**, *139* (5), 1726-1729. DOI: 10.1021/jacs.6b09873.
(76) Denmark, S. E.; Nishide, K.; Faucher, A. M. On the generation and configurational stability of (2S,3S)-1,2,3-triphenylborirane. *Journal of the American Chemical Society* **1991**, *113* (17), 6675-6676. DOI: 10.1021/ja00017a050.
(77) Baik, C.; Hudson, Z. M.; Amarne, H.; Wang, S. Enhancing the Photochemical Stability of N,C-Chelate Boryl Compounds: C−C Bond Formation versus C═C Bond cis,trans-Isomerization. *Journal of the American Chemical Society* **2009**, *131* (40), 14549-14559. DOI: 10.1021/ja906430s.
(78) Rao, Y.-L.; Amarne, H.; Zhao, S.-B.; McCormick, T. M.; Martić, S.; Sun, Y.; Wang, R.-Y.; Wang, S. Reversible Intramolecular C−C Bond Formation/Breaking and Color Switching Mediated by a N,C-Chelate in (2-ph-py)BMes2 and (5-BMes2-2-ph-py)BMes2. *Journal of the American Chemical Society* **2008**, *130* (39), 12898-12900. DOI: 10.1021/ja8052046.
(79) Rao, Y. L.; Chen, L. D.; Mosey, N. J.; Wang, S. Stepwise intramolecular photoisomerization of NHC-chelate dimesitylboron compounds with C-C bond formation and C-H bond insertion. *J Am Chem Soc* **2012**, *134* (26), 11026-11034. DOI: 10.1021/ja304211v.
(80) Braunschweig, H.; Claes, C.; Damme, A.; Deissenberger, A.; Dewhurst, R. D.; Horl, C.; Kramer, T. A facile and selective route to remarkably inert monocyclic NHC-stabilized boriranes. *Chem Commun (Camb)* **2015**, *51* (9), 1627-1630. DOI: 10.1039/c4cc09036e.
(81) Dai, W.; Geib, S. J.; Curran, D. P. Ring-Opening Reactions of NHC-Boriranes with In Situ Generated HCl: Synthesis of a New Class of NHC-Boralactones. *J Am Chem Soc* **2019**, *141* (8), 3623-3629. DOI: 10.1021/jacs.8b13010.
(82) Wang, H.; Zhang, J.; Xie, Z. Ring-opening and ring-expansion reactions of carborane-fused borirane. *Chem Sci* **2021**, *12* (39), 13187-13192. DOI: 10.1039/d1sc04453b.
(83) Wang, J.; Xiang, L.; Liu, X.; Matler, A.; Lin, Z.; Ye, Q. Avenue to novel o-carboranyl boron compounds - reactivity study of o-carborane-fused aminoborirane towards organic azides. *Chem Sci* **2024**, *15* (13), 4839-4845. DOI: 10.1039/d4sc00489b.
(84) Dowd, P. Trimethylenemethane. *Accounts of Chemical Research* **1972**, *5* (7), 242-248. DOI: 10.1021/ar50055a003.
(85) García Ruano, J. L.; Peromingo, M. T.; Martín, M. R.; Tito, A. A New Entry to Enantiopure Polysubstituted Cyclopropanes: Stereoselective Denitrogenation of Sulfinylpyrazolines under Yb(OTf)3 Catalysis. *Organic Letters* **2006**, *8* (15), 3295-3298. DOI: 10.1021/ol061168d.

View Article Online
DOI: 10.1039/D6CP00519E

(86) de Loera, D.; Garcia-Garibay, M. A. Efficient Aziridine Synthesis in Metastable Crystalline Phases by Photoinduced Denitrogenation of Crystalline Triazolines. *Organic Letters* **2012**, *14* (15), 3874-3877. DOI: 10.1021/ol301582n.
(87) Wang, Z.; Wen, J.; Bi, Q.-W.; Xu, X.-Q.; Shen, Z.-Q.; Li, X.-X.; Chen, Z. Oxirane synthesis from diazocarbonyl compounds via NHC-Ag+ catalysis. *Tetrahedron Letters* **2014**, *55* (18), 2969-2972. DOI: 10.1016/j.tetlet.2014.03.105.
(88) Yu, Z.-X.; Wu, Y.-D. An SN2-like Transition State for Alkene Episulfidation by Dinitrogen Sulfide. *The Journal of Organic Chemistry* **2003**, *68* (15), 6049-6052. DOI: 10.1021/jo034027n.
(89) Adam, W.; Bargon, Rainer M. Episulfidation of Strained Cycloalkenes in the Thermolysis of 5-Aryloxy-1,2,3,4-thiatriazoles. *European Journal of Organic Chemistry* **2001**, *2001* (10), 1959-1962. DOI: 10.1002/1099-0690(200105)2001:10<1959::Aid-ejoc1959>3.0.Co;2-n.
(90) Bennie, S. J.; Curchod, B. F. E.; Manby, F. R.; Glowacki, D. R. Pushing the Limits of EOM-CCSD with Projector-Based Embedding for Excitation Energies. *J Phys Chem Lett* **2017**, *8* (22), 5559-5565. DOI: 10.1021/acs.jpclett.7b02500.
(91) Rishi, V.; Perera, A.; Nooijen, M.; Bartlett, R. J. Excited states from modified coupled cluster methods: Are they any better than EOM CCSD? *J Chem Phys* **2017**, *146* (14), 144104. DOI: 10.1063/1.4979078.
(92) Yang, Z.; Jamieson, C. S.; Xue, X.-S.; Garcia-Borràs, M.; Benton, T.; Dong, X.; Liu, F.; Houk, K. N. Mechanisms and Dynamics of Reactions Involving Entropic Intermediates. *Trends in Chemistry* **2019**, *1* (1), 22-34. DOI: 10.1016/j.trechm.2019.01.009.
(93) Frisch, M. J.; Trucks, G. W.; Schlegel, H. B.; Scuseria, G. E.; Robb, M. A.; Cheeseman, J. R.; Scalmani, G.; Barone, V.; Petersson, G. A.; Nakatsuji, H.; et al. Gaussian 16 Rev. B.01. **2016**.
(94) Fdez Galvan, I.; Vacher, M.; Alavi, A.; Angeli, C.; Aquilante, F.; Autschbach, J.; Bao, J. J.; Bokarev, S. I.; Bogdanov, N. A.; Carlson, R. K.; et al. OpenMolcas: From Source Code to Insight. *J Chem Theory Comput* **2019**, *15* (11), 5925-5964. DOI: 10.1021/acs.jctc.9b00532.
(95) Aquilante, F.; Autschbach, J.; Carlson, R. K.; Chibotaru, L. F.; Delcey, M. G.; De Vico, L.; Fdez Galvan, I.; Ferre, N.; Frutos, L. M.; Gagliardi, L.; et al. Molcas 8: New capabilities for multiconfigurational quantum chemical calculations across the periodic table. *J Comput Chem* **2016**, *37* (5), 506-541. DOI: 10.1002/jcc.24221.
(96) Mejia-Rodriguez, D.; Apra, E.; Autschbach, J.; Bauman, N. P.; Bylaska, E. J.; Govind, N.; Hammond, J. R.; Kowalski, K.; Kunitsa, A.; Panyala, A.; et al. NWChem: Recent and Ongoing Developments. *J Chem Theory Comput* **2023**, *19* (20), 7077-7096. DOI: 10.1021/acs.jctc.3c00421.
(97) Greiner, J.; Gianni, I.; Nottoli, T.; Lipparini, F.; Eriksen, J. J.; Gauss, J. MBE-CASSCF Approach for the Accurate Treatment of Large Active Spaces. *J Chem Theory Comput* **2024**, *20* (11), 4663-4675. DOI: 10.1021/acs.jctc.4c00388.

View Article Online
DOI: 10.1039/D6CP00519E

Data and code availability

• The ML-photodynamics simulation code is open-sourced and released at: https://github.com/mlcclab/PyRAI2MD-hiam.

• The complete quantum mechanical data and initial conditions can be found at: 10.6084/m9.figshare.29294228